Article

Geological Study Based on Multispectral and Hyperspectral Remote Sensing: A Case Study of the Mahuaping Beryllium–Tungsten Deposit Area in Shangri-La

Yunfei Hu [1,2,3,4,5], Zhifang Zhao [2,3,4,5,6,*], Xinle Zhang [7], Lunxin Feng [2,3,4,5,6], Yang Qin [1,2,3,4,5], Liu Ouyang [1,2,3,4,5] and Ziqi Huang [1,2,3,4,5]

1   Institute of International Rivers and Eco-Security, Yunnan University, Kunming 650050, China; huyunfei9905@163.com (Y.H.); qinyang@stu.ynu.edu.cn (Y.Q.); oyl0918@163.com (L.O.); huangziqi@stu.ynu.edu.cn (Z.H.)
2   Key Laboratory of Sanjiang Metallogeny and Resources Exploration and Utilization, Kunming 650051, China; fenglunxin@stu.ynu.edu.cn
3   Yunnan Key Laboratory of Sanjiang Metallogeny and Resources Exploration and Utilization, Kunming 650051, China
4   Research Center of Domestic High-Resolution Satellite Remote Sensing Geological Engineering, Kunming 650050, China
5   Yunnan International Joint Laboratory of China-Laos-Bangladesh-Myanmar Natural Resources Remote Sensing Monitoring, Kunming 650050, China
6   School of Earth Sciences, Yunnan University, Kunming 650050, China
7   Geological Science Research Institute of Yunnan Province, Kunming 650000, China; zzxxll51789@163.com
*   Correspondence: zzf_1002@126.com; Tel.: +86-138-8896-5615

Abstract: This study applied Advanced Spaceborne Thermal Emission and Reflection Radiometer (ASTER) multispectral data and ZY1-02D hyperspectral data to map the structural distribution and hydrothermal alteration in the polymetallic ore district in southern Shangri-La City, Yunnan Province, China. The study area hosts several polymetallic deposits, including the Mahuaping tungsten–beryllium deposit, which has significant mineral exploration potential. The deposit type is mainly magmatic–hydrothermal, with average grades of 0.41% WO_3 and 0.22% BeO, and substantial reserves, prominently controlled by faults. Based on this, this study employed ASTER data for the visual interpretation of structures through false-color composites combined with DEM data. Additionally, ASTER and ZY1-02D data were processed using the principal component analysis and spectral angle mapper methods to extract anomalies related to tungsten mineralization such as carbonate alteration, sericitization, chloritization, and hematization of the hydrothermal origin. The results indicated that the structural trends in the study area predominantly align in north–south and northeast directions, with alteration anomalies concentrated in the central and fold areas. Our analysis of typical deposits revealed their close association with north–south faults and east–west joints, as well as the enrichment level of alteration anomalies, identifying five high-potential target areas for mineral exploration. Further evaluation involved field validation through the spectral scanning of samples, field verification, and a comparison with known lithology. These assessments confirmed that the spectral curves matched those in the USGS database, the structural interpretations aligned with the field observations (84% accuracy from 25 sampling points, with 21 matching extracted alteration types), and the alteration results corresponded well with the lithological units, indicating high accuracy in alteration extraction. Finally, a comparative discussion highlighted that the results derived from ZY1-02D data were more applicable to the local area. The outcomes of this study can support subsequent mineral exploration efforts, enhancing the sustainability of important mineral resources.

Keywords: Mahuaping tungsten–beryllium deposit; Yunnan province; multispectral–hyperspectral analysis; magmatic–hydrothermal deposits; structural alteration mapping; mineralization prediction

1. Introduction

Remote sensing plays a crucial role in mineral resource prediction and exploration, integrating geological, geophysical, geochemical, and remote sensing data [1]. The theoretical basis of remote sensing lies in electromagnetic radiation, and the spectral radiation characteristics of objects are the main basis for remote sensing technology to identify and differentiate by measuring the spectral information of minerals. The application of remote sensing in mineral exploration dates back to early studies overseas [2,3]. Typically, remote sensing interpretation relies on terrain texture, color, and other visual features, necessitating high image quality and expertise from researchers. Currently, remote sensing for mineral exploration often utilizes alteration information extraction techniques. By analyzing the spectral characteristics of selected minerals, target areas of interest can be identified [4–7].

Modern multispectral remote sensing data, such as those from ASTER (Advanced Spaceborne Thermal Emission and Reflection Radiometer), are widely used in remote sensing interpretation. Since its launch in 1999, ASTER has been instrumental in geological and mineral exploration due to its high-resolution spectral imaging capabilities and infrared data [8,9]. Advancements have also brought high-spatial-resolution hyperspectral data into play. For instance, China's ZY1-02D satellite, launched with a spatial resolution as low as 1 m and a spectral resolution of 10 nanometers, operates on a data acquisition cycle of approximately seven days [10]. Despite its extensive use in mineral exploration, there remains a scarcity of studies specifically dedicated to extracting hydrothermal alteration information using these advanced datasets.

Therefore, future research in remote sensing for mineral exploration should not only refine data processing and interpretation algorithms, but also explore and utilize new high-precision hyperspectral data to enhance the accuracy and efficiency of mineral resource predictions.

For multispectral data, the band ratio method and principal component analysis (PCA) are commonly used techniques. The band ratio method calculates ratios between different bands to eliminate effects such as illumination and atmospheric scattering, effectively enhancing and highlighting specific spectral characteristics of materials [11,12]. PCA is a widely used technique for data dimensionality reduction and analysis in remote sensing.

Current research on high-spectral-resolution mineral alteration extraction can be broadly classified into three aspects based on the study of spectral characteristic information: the parameterization of spectral features, statistical learning methods, and spectral feature matching [13].

The accurate identification of altered minerals based on spectral feature parameters relies on effectively extracting spectral absorption characteristics, which imposes high environmental requirements [14,15]. Machine learning techniques adaptively model relationships between inputs and outputs, particularly advantageous in handling nonlinear high-dimensional data. However, they heavily depend on the quality and quantity of training samples, which determines the accuracy of the results [16,17]. Spectral feature matching involves selecting spectral libraries or field-measured spectra as reference spectra and directly identifying spectral characteristics of land cover in hyperspectral data using various spectral metrics and matching criteria [18], with the spectral angle method being particularly advantageous.

The Mahuaping area has been evaluated for tungsten and beryllium polymetallic mineral exploration potential, identified mainly as high- to medium-temperature magmatic–hydrothermal-vein-type tungsten–beryllium deposits [19]. The ore-forming temperature in the study area is approximately 350 °C to 151 °C [20]. The mineralization bodies are significantly controlled by faults, occurring as vein-like and fissure-like distributions along them, with minerals such as calcite, dolomite, chlorite, and sericite commonly present within the ore bodies [21–23].

However, the area's rugged terrain, with elevations ranging from 3400 m to 4050 m, and challenging accessibility make traditional exploration methods resource-intensive. This is where the advantages of remote sensing for exploration, such as independence from terrain influence, large coverage, and lower costs, can be effectively utilized. Moreover, previous studies in this area have primarily focused on ore-forming mechanisms, fluid inclusions [24], geochemical characteristics, and mineralization structures [25], with limited exploration using multispectral and hyperspectral remote sensing technologies [26].

Therefore, this study aims to explore and summarize a set of alteration information extraction and mineral exploration methods suitable for harsh mountainous canyon environments like Mahuaping. Using ASTER, visual interpretation was conducted to delineate linear and circular structures in the study area. ZY1-02D data, processed using spectral angle methods, and ASTER data, through principal component analysis, were employed to extract alteration anomaly information, including the carbonate alteration, sericitization, chloritization, and iron staining types.

Subsequently, field verification involved on-site rock sample collection to validate the interpreted structural and alteration extraction results. The close match between the actual scanned mineral spectral curves and those in the spectral library used confirms the obtained results [27]. Minerals such as scheelite and sericite were observed under a polarizing microscope, verifying the high accuracy of the alteration extraction in this study. Based on our research findings, a mineralization model for the region can be constructed to explore potential ore-bearing target areas [28]. The delineation of these five target areas provides significant guidance for subsequent fieldwork.

2. Geological Overview

2.1. Regional Geological Overview

The India–Asia collision began 65 million years ago (Ma), triggering a series of tectonic and magmatic activities, along with mineralization responses, in the Sanjiang region. The research area of this study is located at the junction of the Tibet–Sanjian orogenic belt and the Upper Yangtze Block, spanning four major tectonic units: the Middle Zan Microcontinent, the Yidun Island Arc southern segment (Geza Island Arc), the Garze-Litang Junction Belt, and the western margin of the Yangtze Block, encompassing the Yanyuan–Lijiang Depression Belt (Figure 1). This geological setting hosts a variety of mineral resources, including Cu-Au, Cu-W-Mo, and Pb-Zn deposits, among others. The study area experienced two phases of tectonic stress. The first phase occurred during the early to late Eocene at the onset of the Himalayan Movement I, characterized by predominantly east–west horizontal compression, resulting in the formation of the Tiger Leaping Gorge anticline (Figure 2) and the SN shear fault zone. The second phase occurred during the mid–late Himalayan period, characterized by intense vertical uplift, causing the originally formed SN faults from compression thrust to transform into normal slip-extensions, forming a series of ore-controlling structures. Under such tectonic influences, the Sanjiangkou–Jianchuan deep fault was generated, with its southern and northern segments trending NNE and the central segment NNW, forming a distinctive Z-shaped pattern. The Mahuaping ore deposit is located precisely at the bend of this fault trend.
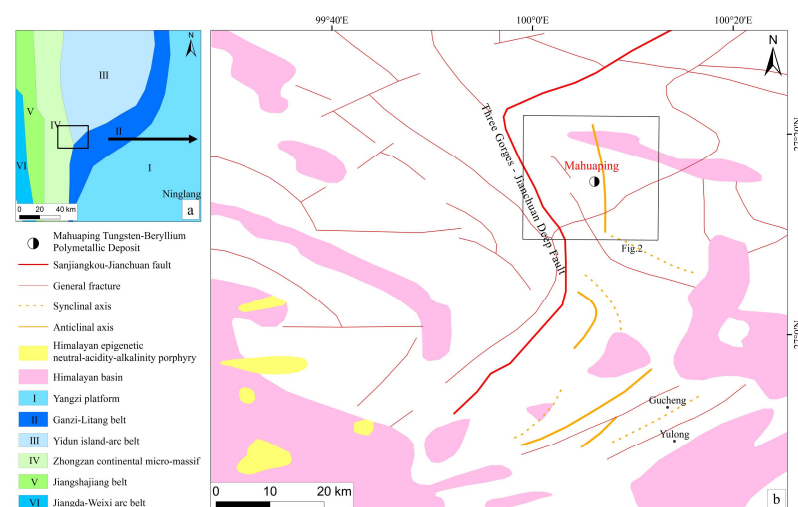

Figure 1. Regional geology and tectonics of the study area: (**a**) Shangri-La region tectonics [29]. (**b**) Mahuaping region tectonics [30].
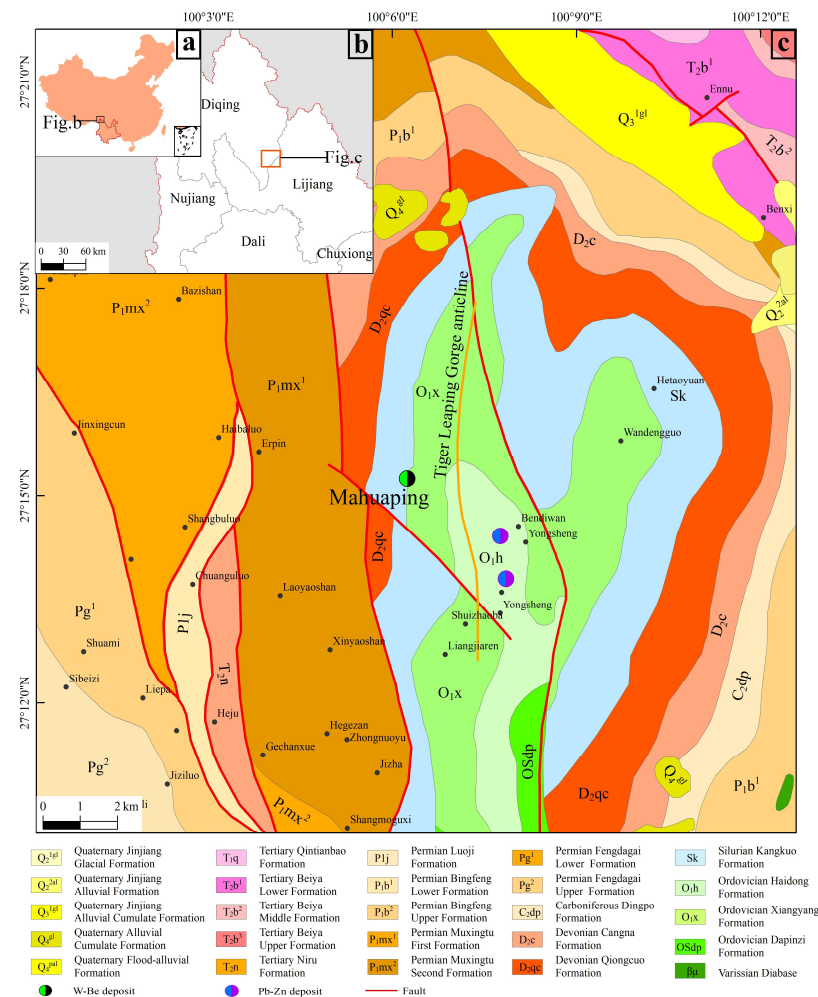
Figure 2. Geological sketch map of Mahuaping area. (**a**) Location of the northwestern part of Yunnan Province, China; (**b**) Location of the study area; (**c**) Geological sketch map of Mahuaping area.

2.2. Geological Overview of the Mahuaping Mining Area

The study area is located at the junction of Deqin Prefecture and Lijiang City in the northwestern part of Yunnan Province, China. The Mahuaping tungsten–tin deposit is situated on the western limb near the axis of the SN Tiger Leaping Gorge anticline (Figure 2). The core of the anticline consists of the Ordovician Haidong Formation, with Ordovician, Silurian, Devonian, and Permian strata occurring sequentially on its flanks, totaling a thickness of nearly 10,000 m (>9662 m). Within the Mahuaping mining area, the predominant outcrops consist of shallow metamorphic rocks from the Lower Devonian and Middle to Upper Devonian limestone formations.

(1) Lower Devonian low-grade metamorphic clastic rocks (D_1): The lower section consists of a suite of metamorphic fine sandstone–metamorphic siltstone, predominantly interbedded with ribboned phyllites, and laminated fine metamorphic siltstones, with metamorphic siderite quartz siltstones. The top section includes interbedded metamorphic calcareous phyllite siltstone, lensoidal marbleized gray sandstone, and metamorphic siderite quartz siltstone. The upper section comprises gray to gray-black siltstone phyllites interbedded with carbonaceous phyllites, calcareous phyllites, and lensoidal marbleized schists. The rocks exhibit banded marbleized schists.

(2) Middle to Upper Devonian marble (D_{2+3}): Mainly light gray to gray-white thin to medium-thick layers, composed of partially blocky marbles interspersed with dark gray marbleized limestone. The lower part contains banded or lensoidal marbleized dolomitic limestone, with localized interbeds of metamorphic carbonaceous siltstone

in the middle part. The top part consists of bioclastic rocks, metamorphic carbonaceous muscovite siltstone, and carbonaceous phyllites.

The surrounding rocks exhibit significant alteration characterized by silicification, pyritization, sericitization, carbonatization, sericite–fluorite alteration, and decolorization alteration. Silicification is common in the dolomites or lower part of the clastic rocks near the tungsten deposits or alongside quartz veins; pyritization is impregnated in the metamorphic clastic rocks of the Lower Devonian and dolomites of the Middle to Upper Devonian. Dolomites near the ore bodies commonly exhibit carbonatization and decolorization alteration, with calcite veins and nodules developed in the veins; sericite and fluorite are the main hydrothermal alteration minerals, often occurring together without clear boundaries, generally appearing as vein-like occurrences; due to hydrothermal action, dolomites near ore bodies and dolomitized limestone commonly undergo recrystallization, resulting in decolorization into white micro-fine crystalline dolomites.

The mineralization of the Mahuaping tungsten–tin deposit mainly contains scheelite, wolframite, galena, and sphalerite. Altered minerals primarily include sericite, fluorite, quartz, chlorite, biotite, pyrite, and calcite. Surface-exposed quartz veins and sericite–fluorite veins locally display tungsten–tin mineralization, serving as direct exploration indicators.

3. Data and Methods

This study utilized ZY1-02D and ASTER data to visually interpret linear and circular structures. It employed principal component analysis and spectral angle mapping to extract alteration information (Figure 3). Building upon existing data, the study summarized the remote sensing geological features of the ore deposit and ultimately delineated prospective exploration targets.
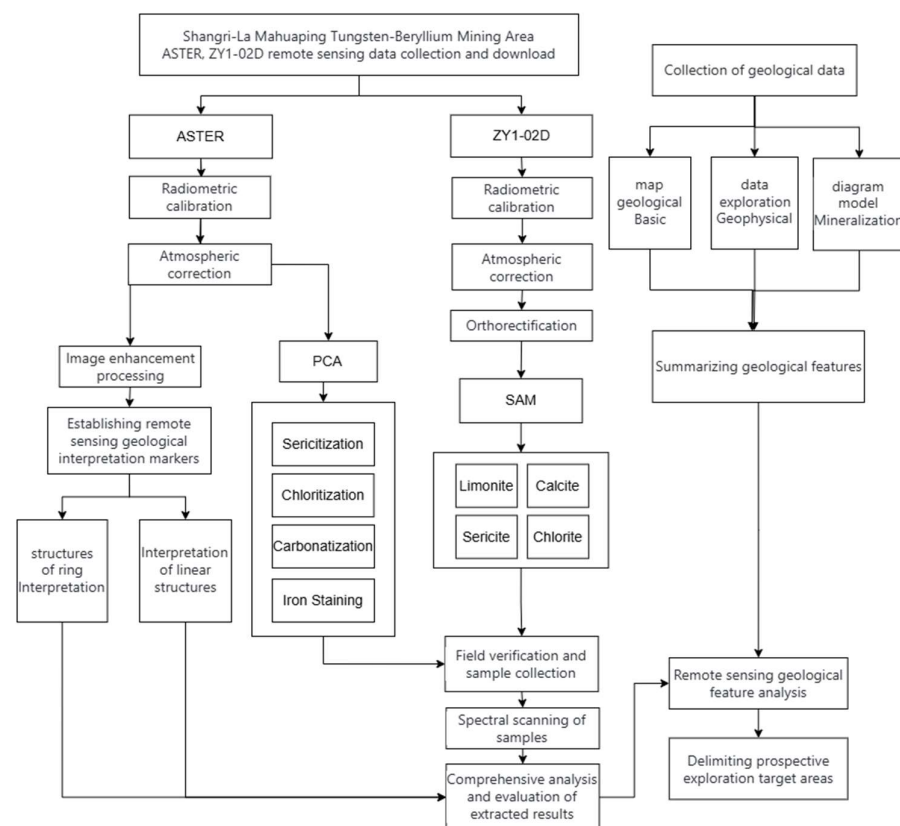

Figure 3. Technical roadmap.

ZY1-02D comprises hyperspectral data with a high spectral resolution, offering significant advantages in the field of mineral alteration extraction, particularly in areas unique to

China and that are less studied. ASTER data include four bands with a spatial resolution of 15 m, which can be used for structural analysis and interpretation. Comparisons can be made between these bands and ZY1-02D to explore differences in mineral alteration information extraction between the two datasets.

3.1. Utilizing the Data

ASTER is an advanced optical sensor on the Terra satellite, a collaboration between NASA and Japan's Ministry of Economy, Trade, and Industry (METI), with active participation from both countries' scientific and industrial sectors. It includes 14 spectral channels from visible to thermal infrared (Table 1) [31], providing scientific and practical satellite data for various fields of Earth environmental resource research. Based on this foundation, Mahdi et al. [32], Abubakar et al. [33], and Ghosh et al. [34] utilized ASTER data to study mineral alteration zones in selected regions. The ASTER data for this study were obtained from USGS EarthExplorer, consisting of two images captured on 23 November 2000 and 6 October 2000.

Table 1. Parameters of utilized data.

Item		Terra (ASTER)	ZY1-02D (AHSI)
Spectral range			
		0.52~0.60 µm	0.396–1.04 µm (b1–b76)
	VL/NIR	0.63~0.69 µm	
		0.76~0.86 µm	
		1.60~1.70 µm	1.005–2.501 µm (b77–b166)
		2.145~2.185 µm	
		2.185~2.225 µm	
	SWIR	2.235~2.285 µm	
		2.295~2.365 µm	
		2.360~2.430 µm	
		8.125~8.475 µm	Null
		8.475~8.825 µm	
	TIR	8.925~9.275 µm	
		10.25~10.95 µm	
		10.95~11.65 µm	
	PAN		
Spatial resolution	VL/NIR	15 m	30 m
	SWIR	30 m	
	TIR	90 m	
	PAN	Null	
Spectral resolution	VL/NIR	Null	10 nm
	SWIR		20 nm
	TIR		Null
	PAN		

The ZY-1 02D satellite (5 m optical satellite) was successfully launched on 12 September 2019. It is China's first independently developed and operated hyperspectral business satellite. Equipped with two cameras, it can effectively capture 9 spectral bands of multispectral data over a swath width of 115 km, and 166 spectral bands of hyperspectral data over a swath width of 60 km. The data for this study were obtained from the Yunnan Remote Sensing Center, China, comprising one image captured on 29 October 2021.

Using Envi 5.6 remote sensing image processing software, the preprocessing of ASTER L1T data involves radiometric calibration, atmospheric correction, and image enhancement. For ZY1-02D AHSI L1 data, radiometric correction, bad pixel repair, and spectral correction have been performed, but systematic geometric correction has not been carried out. However, correction can be achieved using the RPC (Rational Polynomial Coefficients) file provided and referencing other image data as needed. Preprocessing requires radiometric calibration, atmospheric correction, and orthorectification (Figure 4).
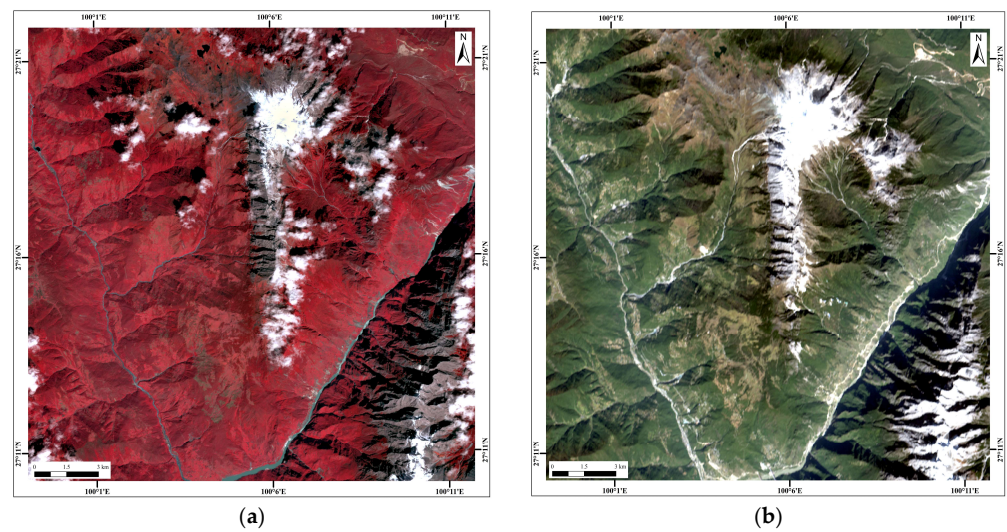
(**a**) (**b**)

Figure 4. Preprocessed remote sensing images: (**a**) ASTER Image 321. (**b**) ZY1-02D Image 29-19-10.

3.2. Method

3.2.1. Structural Interpretation

Using satellite remote sensing technology for interpretation requires geological features to be reflected primarily in remote sensing images through aspects such as tone, shape, and texture. In remote sensing geology, these are manifested as linear structures, circular structures, and other signatures [35]. The Mahuaping tungsten–tin deposit is situated in an area where tectonic activities are generally intense, characterized by prominent faults, folds, and joints. It has undergone multiple episodes of superimposed tectonic activities, with frequent volcanic activities creating necessary conditions for ore-forming hydrothermal fluids [36]. This suggests that regions with a higher distribution of such structures are more likely to contain mineral deposits. Therefore, if structural interpretations frequently appear in a particular area, subsequent prospecting efforts should prioritize these areas. Structural interpretation in this study utilizes ASTER remote sensing imagery, enhanced through principal component analysis. Based on established interpretation criteria (Table 2), structural interpretation work in the Mahuaping mining area has commenced.

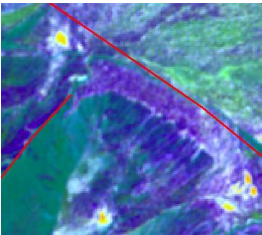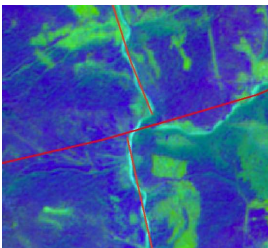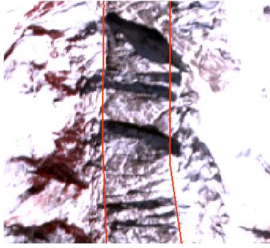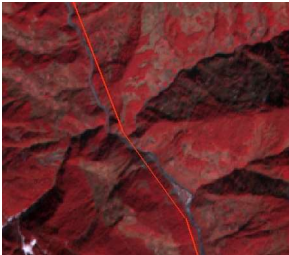**Table 2.** Structural interpretation markers for Mahuaping mining area.
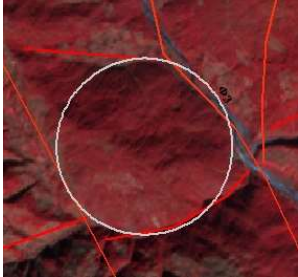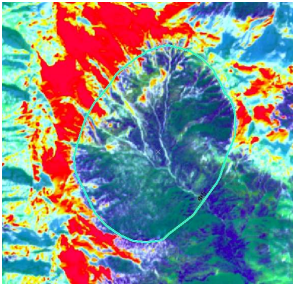
Interpretation Marker	Type	Data/Method Used	Description Characteristics
	Fault	Principal component analysis of bands 1, 2, 3, and 4 (RGB: pc1, pc3, pc4)	A sizable colored line or colored boundary
	Fault	Principal component analysis of bands 1, 2, 3, and 4 (RGB: pc1, pc3, pc4)	Anomalous watercourse abruptly bends at right angles, then resumes its original direction and continues extending

Interpretation Marker	Type	Data/Method Used	Description Characteristics
	Fault	ASTER (RGB: 321)	Translated linear extension imagery with patchy or mottled patterns, characterized by fine textures within the area, featuring fragmented blocks often appearing as small patches
	Fault	ASTER (RGB: 321)	Translated mountain ridge faults and mountain displacement, where in parts of the mountain range originally oriented northeast, there are local dislocations. The continuous ridge is offset
	Magmatic ring	ASTER (RGB: 321)	Translated circular structure caused by volcanic activity. The large ring is composed of multiple cycles of rings, while the small rings often appear obscure. These volcanic rings indicate past underground magma activity in the area
	Structural ring	ASTER (RGB: 321)	Structural rings often remain intact in the middle despite being cut by fault structures around them, forming features with nearly circular patterns
	Intrusive rock formation ring	Principal component analysis of bands 1, 2, 3, and 4 (RGB: pc1, pc3, pc4)	Translated intrusive rocks, which are magma products that have not surfaced in the region, closely related to underground rock bodies. They exhibit a distinct center, with radial fractures and joints around them, resembling a radial bursting pattern

3.2.2. Alteration Information Extraction

The characteristic spectral features of rock minerals form the basis for lithological interpretation, and the reliability of extraction results depends on analyzing the spectral curves of altered characteristic minerals. The selected characteristic minerals for this study were sericite, chlorite, calcite, and goethite. A portable near-infrared mineral analyzer developed by the Nanjing Institute of Geology and Mineral Resources was employed, with

a scanning spectral wavelength range of 350 to 2500 nm and a spectral resolution of 2 nm. Field samples from the Mahuaping mining area were spectrally measured on site.

From the scanned spectral curves, smooth and continuous curves matching the spectral characteristics of sericite, chlorite, and calcite were selected (Figure 5). However, due to the instrument's inability to capture the absorption features of goethite within the scanned spectral range, it was not possible to distinguish goethite using this mineral analyzer. Therefore, the spectral curve for goethite is absent. For the subsequent extraction of alteration information related to goethite, spectral curves from the US Geological Survey (USGS) were utilized for analysis.
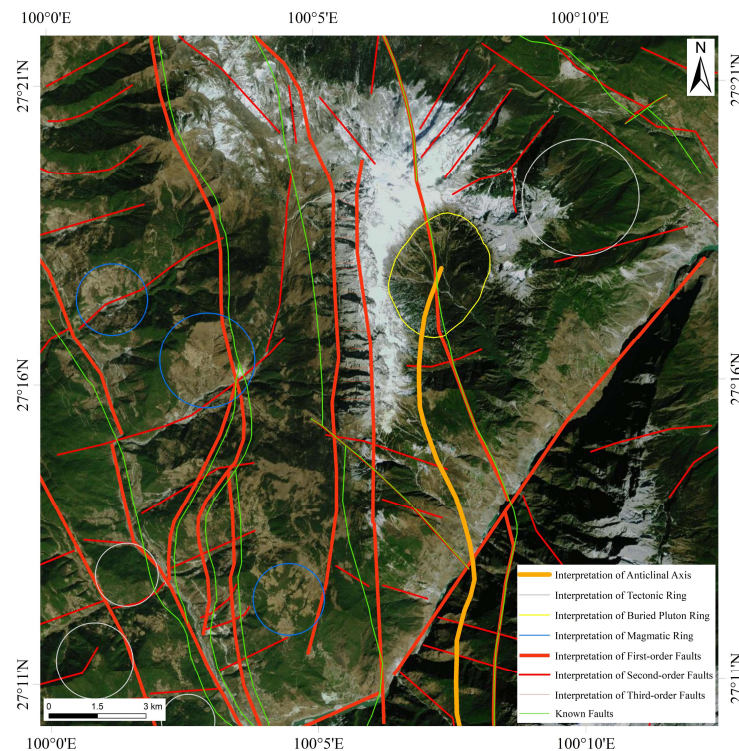

Figure 5. Structural interpretation map of linear and circular structures in the study area.

After determining the absorption features of the measured spectral curves, this study employed ASTER for principal component analysis (PCA) and ZY1-02D for spectral angle mapping (SAM) research. Spectral angle mapping extracts alteration information for individual minerals, while principal component analysis extracts alteration information for specific mineral groups. By overlaying these two results, their respective strengths can complement each other, enhancing the overall outcome [37,38].

Principal component analysis (PCA) is one of the commonly used methods for extracting the alteration information of surrounding rocks [39,40]. PCA involves performing correlation statistical analysis on the raw multispectral images generated by multiple spectral channels, producing a set of linearly uncorrelated combinations of the original input images—principal components [41]. Useful information from various bands is compressed into the first few principal components, achieving decorrelation and allowing the enhancement effect of specific principal components on the spectral characteristics of ground objects to be assessed. Using this method, scholars such as Abdelkareem et al. [42] and Gabr et al. [43] have refined different lithological units using PCA and other techniques. Honarpazhouh et al. [44] employed PCA and hierarchical clustering analysis to compress information into a few maps, aiding in the determination of multi-element associations with good results. This study utilized the PCA method with Envi 5.6. To perform PCA, we must perform the following steps: Open the remote sensing image in Envi, and activate

the PCA module ("Forward PCA Rotation New Statistics and Rotate"). Select the spectral bands corresponding to altered minerals, and specify the output location for the results and the Statistics File. Use the module ("View Statistics File") to examine the feature vector matrix. Identify a component that matches the spectral characteristics of altered minerals for density slicing. Choose an appropriate threshold to obtain the final information on the altered minerals.

The spectral angle mapper (SAM) calculates the vector angle between the spectral signatures of pixels within a study area and those in a spectral library, determining the similarity between two spectra and identifying potential mineralized areas [45]. SAM employs spatial feature vectors to characterize each multidimensional spatial point, using the similarity of angular distances between these vectors as a basis for classification, which falls under supervised classification [46]. It requires known reference spectra for each class, typically sourced from databases like the USGS spectral library used in this study. SAM not only finds broad application in land type classification [47], but is also extensively utilized in extracting mineral alteration information [48–56]. Using Envi 5.6, since ZY1-02D data are from Chinese satellites, we must perform the following steps: Download a specific plugin (China Satellites) to open the remote sensing image. In the Spectral Library Viewer, select the appropriate spectral curve for altered minerals. Next, utilize the SAM module (spectral angle mapper classification). Choose the bands involved in the calculation, input suitable thresholds, and generate the output. If the results are not satisfactory, perform density slicing again to obtain the final results.

4. Results

4.1. Structural Interpretation Results

In this structural interpretation project, a total of 55 linear structures were interpreted, including faults and joints. Among them, there are 34 faults trending in the NE direction, 7 faults trending approximately N-S, and 14 faults trending in the NW direction. There are three volcanic rings, three tectonic rings, and one concealed rock mass ring.

Through a comparison with known faults, these linear structures interpreted to coincide or closely coincide with known structures are defined as fault structures, while the rest are categorized as remotely sensed interpreted linear faults.

The mineralization of the Mahuaping tungsten–beryllium deposit is primarily controlled by the transverse tension fractures and shear fractures trending nearly east–west, which are associated with the local Wan anticline and the western wing of the anticline. The degree of fracture development is closely related to the strength of mineralization, showing a proportional relationship: stronger mineralization is observed where fractures are well developed. According to the interpreted structural rings (Figure 5), areas with structural clustering exhibit higher potential for mineralization.

4.2. Principal Component Analysis (PCA)

To match the spectral curves with different sensors, the measured spectral curve (Figure 6a) was resampled to match ASTER (Figure 6b) and ZY1-02D (Figure 6c). Spectral feature analysis was performed on the resampled ASTER spectral curve in specific ranges: 500 nm to 900 nm (Figure 6d) and 2100 nm to 2400 nm (Figure 6e).

Sericite, characterized by its Al-OH content, exhibits absorption features in the sixth spectral band, while showing reflective characteristics in the third band. Carbonate rocks, due to their CO_3^2 content, display strong absorption features at 2.35 μm, corresponding to the eighth band of ASTER data. In ASTER bands 1 to 3, carbonate-bearing minerals exhibit enhanced reflection, forming a peak in the third band and showing weak absorption in the fifth band. For iron-bearing minerals across ASTER bands 1 to 4, reflection is generally enhanced, with peaks corresponding to ASTER bands 2 and 4, and an absorption valley between these two peaks. Chlorite forms absorption valleys in the second and eighth bands of ASTER data.
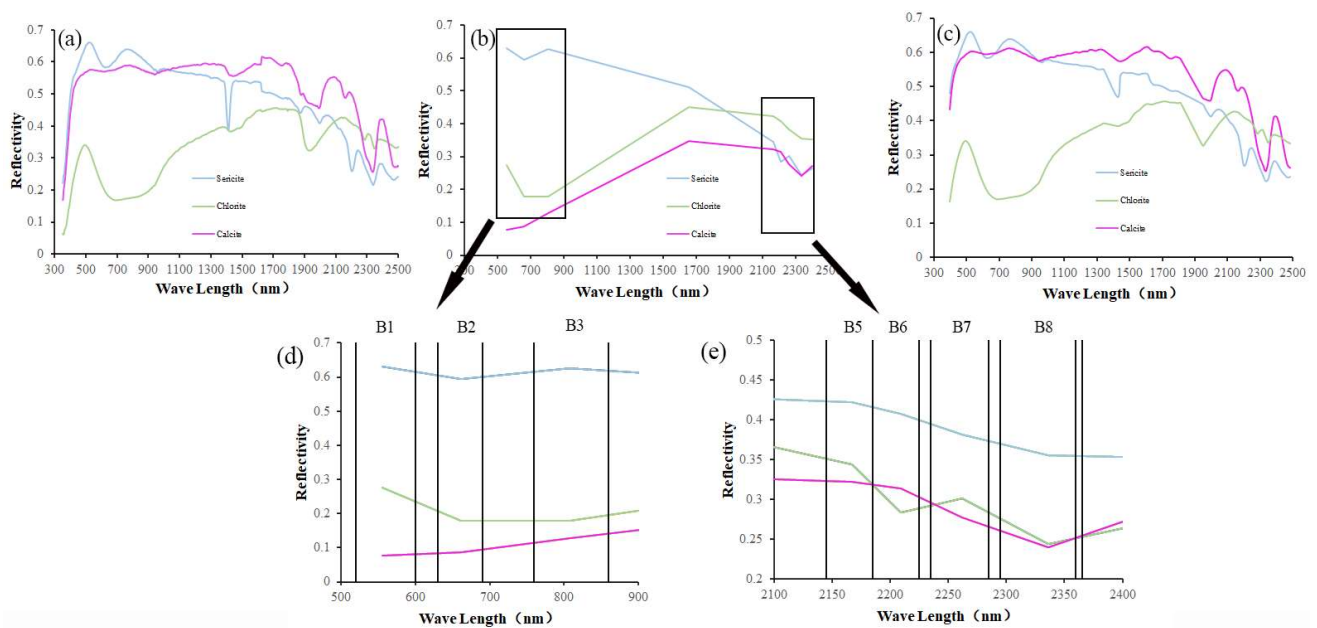
Figure 6. Spectral curves: (**a**) measured spectral curve; (**b**) measured spectral curve resampled to ASTER; (**c**) measured spectral curve resampled to ZY1-02D; (**d**) resampled spectral curve from 500 nm to 900 nm; (**e**) resampled spectral curve from 2100 nm to 2400 nm.

Principal component analysis (PCA) extracted four types of alteration: iron staining [57], sericitization, chloritization, and carbonatization. Each type was analyzed by selecting characteristic spectral segments and choosing the principal components (PCs) that best fit these characteristics (Table 3). PC4 was selected for sericitization, PC2 for carbonatization, PC4 for chloritization, and PC3 for iron staining. RGB color synthesis of the selected principal components for each type (Figure 7) effectively delineated the extent and intensity of weathering processes [58].

Table 3. Principal component analysis feature statistics table: (a) PCA results for sericite alteration. (b) PCA results for carbonate alteration. (c) PCA results for chlorite alteration. (d) PCA results for iron staining.

| (a) Eigenvectors	PC1	PC2	PC3	PC4
Band 1	−0.478906	−0.539819	−0.692171	**−0.011992**
Band 3	−0.814557	−0.020538	0.579694	**−0.005393**
Band 6	−0.230614	0.615599	−0.308632	**−0.68746**
Band 7	−0.2323	0.573769	−0.299333	**0.726104**
(b) Eigenvectors	PC1	**PC2**	PC3	PC4
Band 1	−0.448528	**−0.514381**	−0.719857	−0.126653
Band 3	−0.790672	**−0.152735**	0.58637	0.087638
Band 5	−0.351592	**0.725998**	−0.201973	−0.555443
Band 8	−0.223705	**0.43013**	−0.311742	0.817167
(c) Eigenvectors	PC1	PC2	PC3	**PC4**
Band 1	0.63034	0.204404	0.744642	**0.079998**
Band 2	0.730161	0.17149	−0.656654	**−0.079134**
Band 5	0.194764	−0.727934	0.104675	**−0.649016**
Band 8	0.177776	−0.631603	−0.057944	**0.752407**
(d) Eigenvectors	PC1	PC2	**PC3**	PC4
Band 1	−0.510673	−0.373236	**0.312665**	0.708624
Band 2	−0.596764	−0.30381	**0.248685**	−0.699806
Band 3	−0.617865	0.562234	**−0.542232**	0.090113
Band 4	−0.03646	0.672523	**0.739176**	0.001801
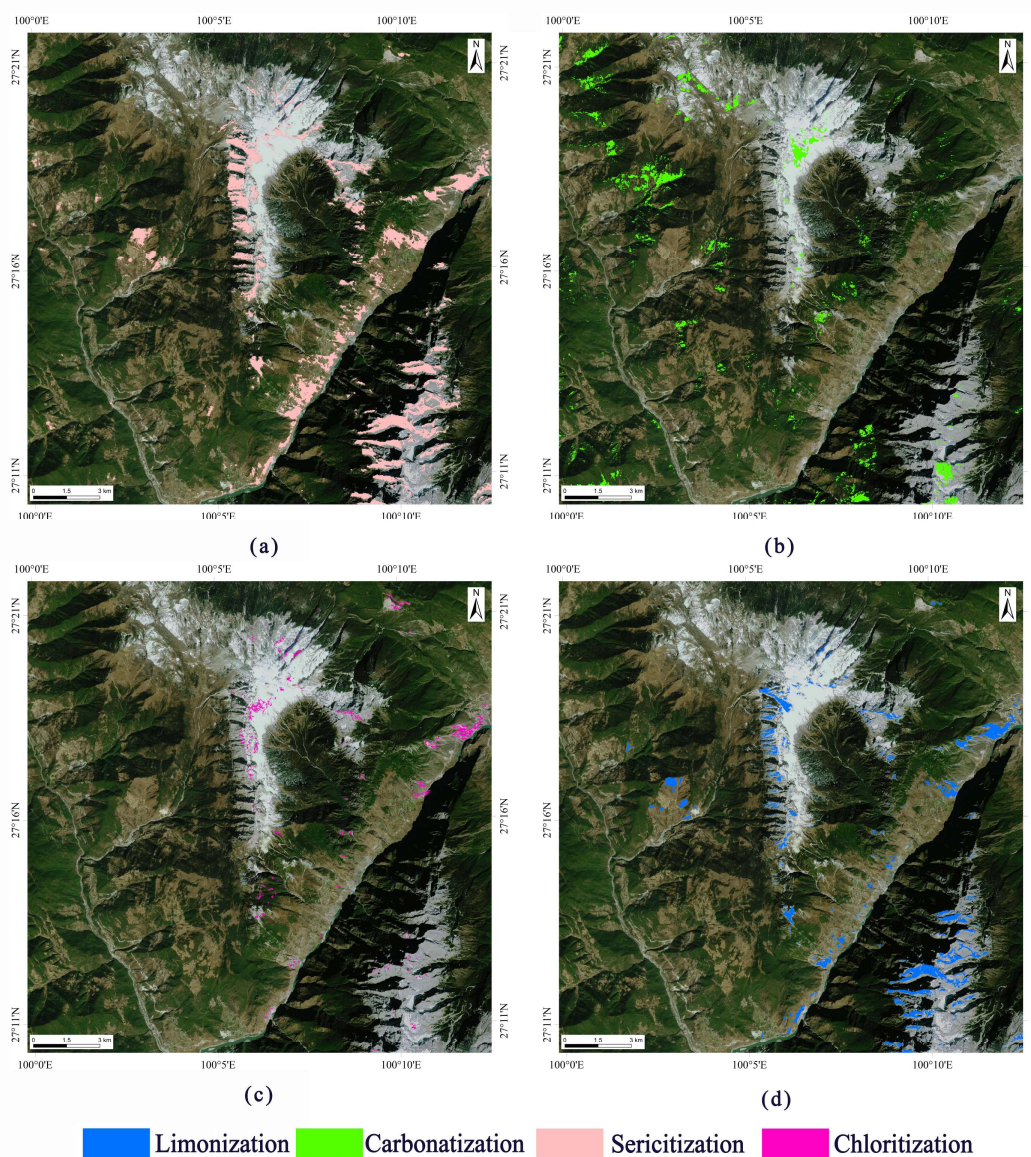
Figure 7. Extraction results of mineral alteration anomalies in Mahuaping mining area: (**a**) sericite alteration; (**b**) carbonate alteration; (**c**) chlorite alteration; (**d**) iron staining.

The mineral alteration zones mostly exhibit dot-, belt-, and block-like distributions. Iron-stained alteration anomalies appear in belt-like patterns (Figure 7a), distributed mainly on ridges and both sides of valleys, with scattered occurrences elsewhere. Carbonatization is predominantly found in the northwest of the study area (Figure 7b). Sericitization alteration anomalies are observed in patchy and belt-like patterns (Figure 7c), occurring not only on ridges but also along both sides of river channels. Chloritization has a relatively small distribution area (Figure 7d).

4.3. Spectral Angle Method (SAM)

In the study area, the typical alteration minerals selected include calcite, limonite, sericite, and chlorite. The spectral curves of these alteration minerals were chosen from the USGS spectral library as reference spectra. The processed images, already subjected to complete preprocessing, were analyzed using spectral angle mapping to obtain the extracted anomaly results (Figure 8). The results from the spectral angle complement the principal component analysis and have indicative significance for delineating target areas later on.
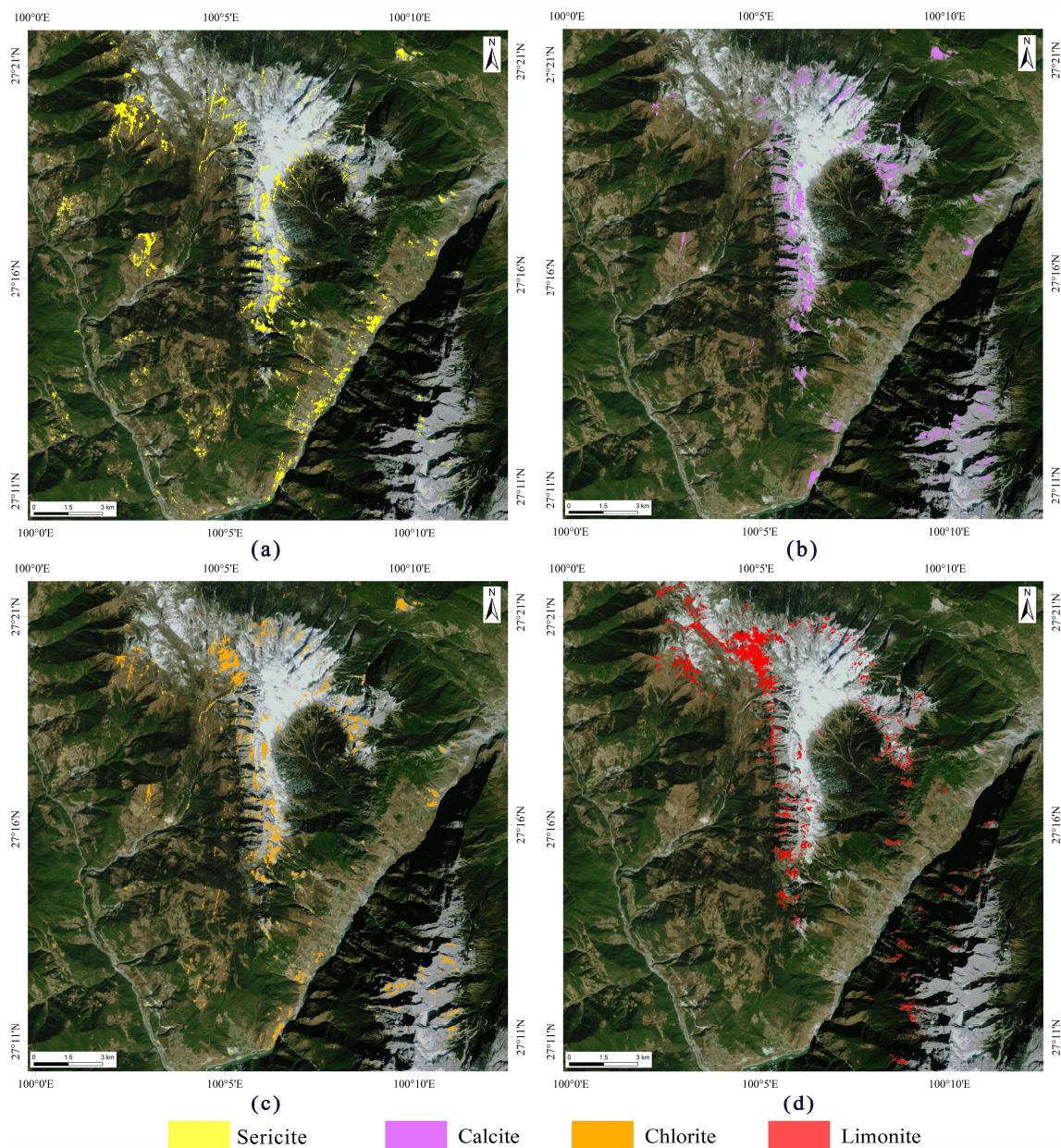
Figure 8. Extraction of alteration anomalies using spectral angle method. (**a**) Sericite; (**b**) calcite; (**c**) chlorite; (**d**) limonite.

4.4. Comprehensive Analysis

Our analysis of the alteration information extraction results (Figure 9) indicates that the Mahuaping mining area exhibits the characteristic of multiple types of remote sensing alteration anomalies overlaid and developed in combination. Various types of wall-rock alterations occur simultaneously, increasing the likelihood of discovering tungsten and beryllium deposits. Taking into account the distribution of structures, five target areas were delineated within these overlapping regions of remote sensing anomalies. The focus of this study is primarily on the area north of the Jinsha River; therefore, the southern region of the Jinsha River is not included in the target area. Alteration information along the northern coast of the Jinsha River is distinct and concentrated; however, due to higher levels of human development along the coast, anthropogenic structures could significantly impact the alteration results and are therefore excluded from the target area.
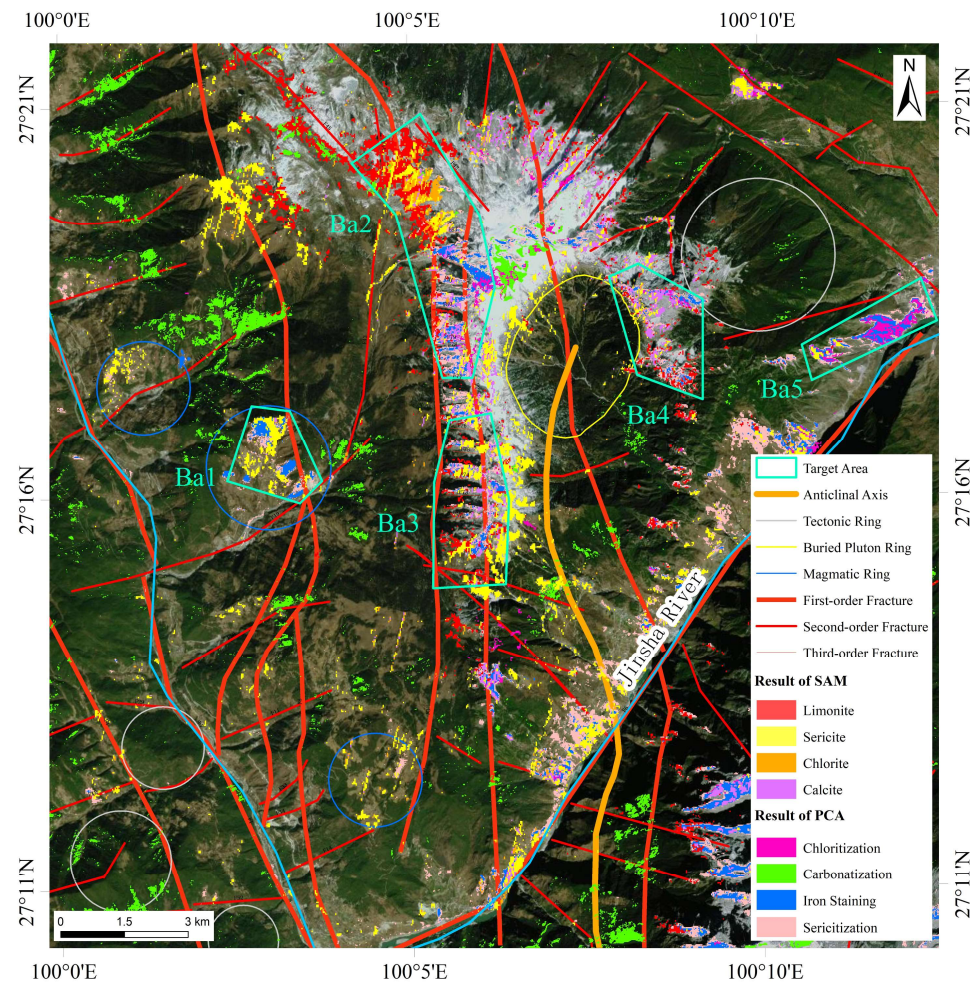
Figure 9. Distribution map of prospective areas for mineralization prediction.

The Ba1 target area is located in the western part of the study area, characterized by well-developed sericite and iron staining alterations, with minor chlorite alteration. These alterations are predominantly blocky in distribution and are situated at the intersection of three faults, which trend approximately north–south. The N-S faults serve as favorable mineralizing structures within the area. The Ba2 and Ba3 target areas are situated on the western flank of the fold axis, similar to typical ore deposits. Multiple primary N-S faults traverse these areas, with transverse fractures developed between two fault structures, making them favorable for ore hosting. Ba2 predominantly exhibits sericite and iron staining alterations, along with significant chloritization and scattered carbonate alterations in vein-like and blocky distributions. Ba3 shows similar conditions but with less widespread iron staining alterations, appearing as scattered dots. Ba4 is adjacent to concealed rock bodies, exhibiting a complete range of alteration types but in a more scattered distribution. The presence of concealed rock bodies suggests potential underlying acidic rock bodies, indicating significant exploration potential. The Ba5 target area, near the Jinsha River, features widespread alterations sandwiched between three faults. Sericite and iron staining alterations are predominant, with significant chloritization also present. These alteration characteristics resemble those of the Mahuaping tungsten–bismuth deposit, suggesting promising exploration prospects.

5. Discussion

5.1. Accuracy of Spectral Scanning Results

The scanning spectrometer used in this study is the CSD-350A wide-band hyperspectral spectrometer developed by the Nanjing Center of China Geological Survey. It offers advantages

such as high efficiency, low cost, and the capability to handle large volumes of data, collecting mineral reflection characteristics within the spectral range of 350 to 2500 nm. Prior to spectral scanning, samples were initially screened visually, and their spectral features were input into the instrument using a probe to generate curves. Mineral identification was then automated using the MSA (v3.6) software, specifically designed for use with the spectrometer, ensuring the accuracy of the spectral curve and mineral correspondence. Spectral curves for sericite, chlorite, and calcite were obtained in this scanning process.

This scan yielded characteristic wavelength positions that are largely consistent with those obtained by other researchers. For sericite, there are two distinct absorption peaks located around 2200 nm and 2350 nm [59], while the measured spectral curve peaks are observed at 2204 nm and 2339 nm. The chlorite spectra exhibit diagnostic absorption features of Fe-OH and Mg-OH, with wavelengths ranging from 2245 to 2260 nm and 2320 to 2360 nm [60]. In the measured spectra, absorption peaks are found at 2286 nm and 2350 nm. Carbonate minerals show prominent absorption features near 2330 nm [61], with measured spectral curve peaks observed at 2336 nm.

The measured spectral curves (Figure 10a) were compared with those from the USGS spectral library (Figure 10b), showing similar overall shapes and matching characteristic band positions. For instance, sericite exhibits an absorption peak at 2203 nm in the USGS library (Figure 10c), while the measured spectral curve shows a peak at 2204 nm (Figure 10d), a difference of 1 nm. Similarly, calcite shows an absorption peak around 2336 nm in the measured curve (Figure 10e) compared to 2338 nm in the USGS curve (Figure 10f), a difference of 2 nm. However, significant discrepancies exist in some characteristic absorption peak positions. For chlorite, the measured peak is at 2286 nm, whereas in the USGS data, it is at 2257 nm, a difference of 29 nm. These discrepancies in peak positions may arise due to the presence of different mineral mixtures in the tested rock samples, as the USGS tests use finely ground pure minerals, which are more accurate for identifying single minerals. In contrast, field samples typically consist of combinations of multiple minerals, making the measured spectral curves more representative of actual conditions in the study area.
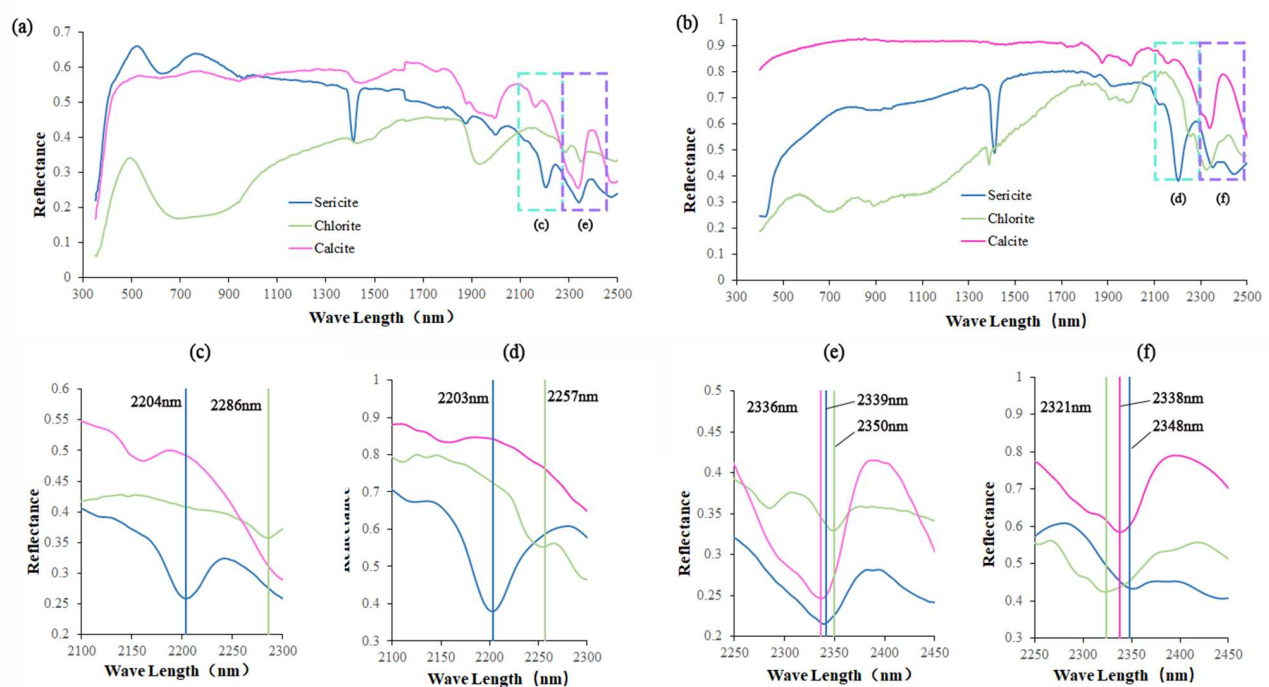

Figure 10. (**a**) Measured spectral curves of alteration characteristic minerals; (**b**) USGS spectral curves of alteration characteristic minerals; (**c**) measured spectral curves in the 2100~2300 nm range; (**d**) USGS spectral curves in the 2100~2300 nm range; (**e**) measured spectral curves in the 2250~2450 nm range; (**f**) USGS spectral curves in the 2250~2450 nm range.

5.2. Accuracy of Extraction Results

Due to the high altitude and rugged terrain in the study area, many target areas are difficult to access. Considering safety and transportation factors, validation points were established as much as possible within the distribution zones of the obtained alteration results (Figure 11). In this fieldwork, 30 validation points were planned, but actually, 42 were established. Additionally, 30 field sampling points were planned, but only 25 were realized (Table 4). Out of these, 21 validation points were correctly matched with the alteration extraction results, demonstrating the accuracy of the alteration information extraction process.
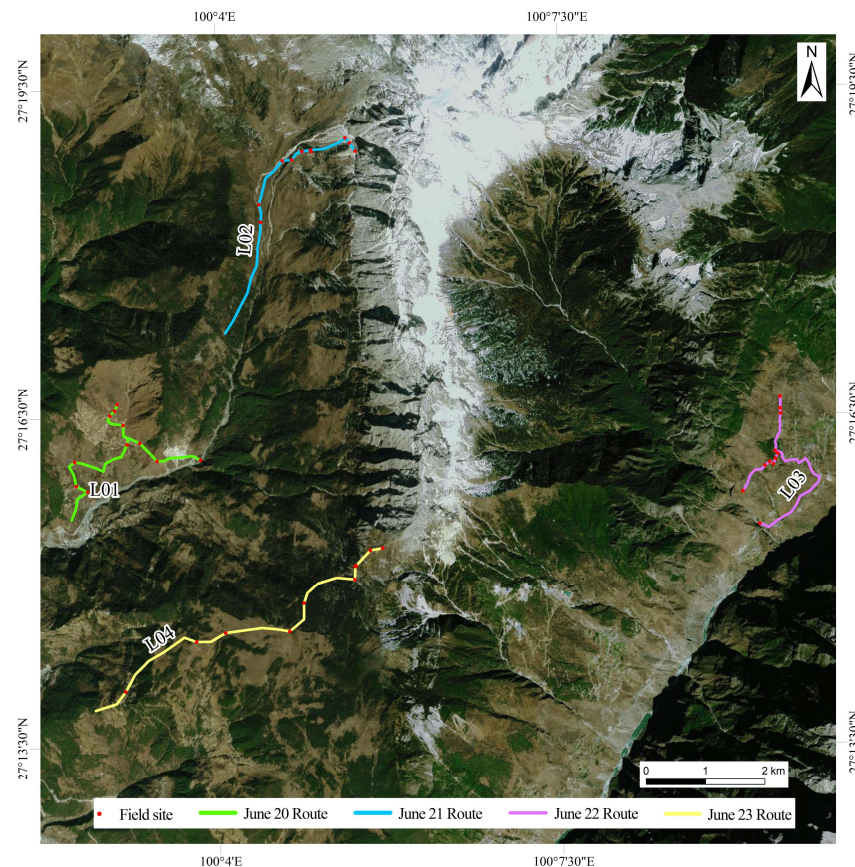

Figure 11. Field survey route map.

Table 4. Sampling points of various field routes.

Line Number	Field Verification Points	Field Sampling Points
L01	1–11	1–10
L02	12–22	16–18, 21
L03	22–32	23, 28–31
L04	33–42	33–38

Through field verification, the L01 survey route revealed extensive sericite alteration (Figure 12a), mostly within sericite schist. Carbonatization was also prevalent, predominantly in carbonate schist (Figure 12b), often accompanied by quartz veins, aligning well with the alteration results. On the L02 survey route, direct observations included scheelite crystals (Figure 12c) and one of the alteration minerals associated with tungsten–beryllium ores, namely blue tourmaline. The scheelite crystals exhibited good crystal forms, albeit small in size, occurring in clusters and showing strong fluorescence under ZGD-8C ultraviolet light (Figure 12d), appearing sky-blue. Limestone was more prevalent along the L03 survey route, featuring karst erosion channels (Figure 12e), while the L04 survey

route revealed chlorite-altered schist (Figure 12f). A total of 42 field survey points were established, with 48 samples collected. Probes from samples numbered 16, 17, 18, 21, 25, 28, 33, and 38 were prepared and examined under polarized light microscopy, confirming the presence of minerals such as quartz, tourmaline, sericite, pyrite, and scheelite (Figure 13), further verifying the high accuracy of the alteration information extraction process.
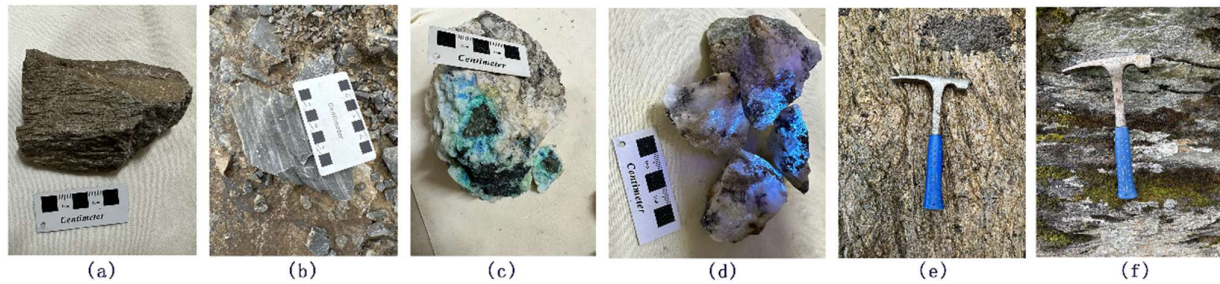

Figure 12. Field collection sample photos: (**a**) Sample 3—sericite feldspar schist; (**b**) Sample 6—carbonate-altered schist; (**c**) Sample 18—lazurite, scheelite; (**d**) scheelite fluorescence reaction; (**e**) Sample 27—marble; (**f**) Sample 37—sericite chlorite schist.
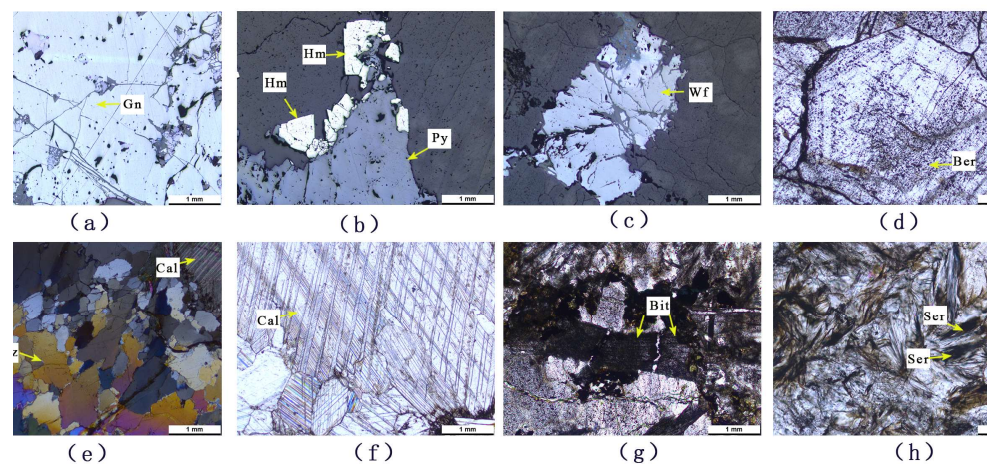

Figure 13. Microscopic identification photos of field samples in the study area (**a**) Sample 16—Gn (galena) 2.5× (reflected light); (**b**) Sample 17—Hm (hematite), Py (pyrite) 2.5× (reflected light); (**c**) Sample 18—Wf (scheelite) 2.5× (reflected light); (**d**) Sample 21—Ber (beryl) 2.5× (single polarization); (**e**) Sample 28—Qtz (quartz) 2.5× (cross-polarized light); (**f**) Sample 28—Cal (calcite) 2.5× (single polarization); (**g**) Sample 33—Bit (biotite) 2.5× (single polarization); (**h**) Sample 38—Ser (sericite) 5× (cross-polarized light).

5.3. Comparison Analysis of Alteration Extraction Results and Lithology

According to the lithological information provided by the geological map, a comparative analysis with the extraction results (Figure 14) reveals finer details beyond what is depicted on the geological map. To enhance visualization, the results from the spectral angle mapper (SAM) were merged with the principal component analysis (PCA) results. Carbonatization alteration is primarily distributed in Permian and Ordovician formations containing various carbonate minerals such as limestone and dolomite. Chlorite alteration predominates in Permian strata, with minor occurrences in tuffaceous and argillaceous shale, often containing pockets of chlorite, consistent with lithological descriptions on the geological map. Sericitization is mainly found in Devonian and Ordovician formations, with Devonian layers comprising sericite schist and carbonaceous sericite slate, and Ordovician layers containing shale with minor sericite content. Iron staining alteration is concentrated in Devonian metamorphic breccia and marble, with widespread occurrences elsewhere, possibly due to surface weathering leading to iron mineral enrichment.
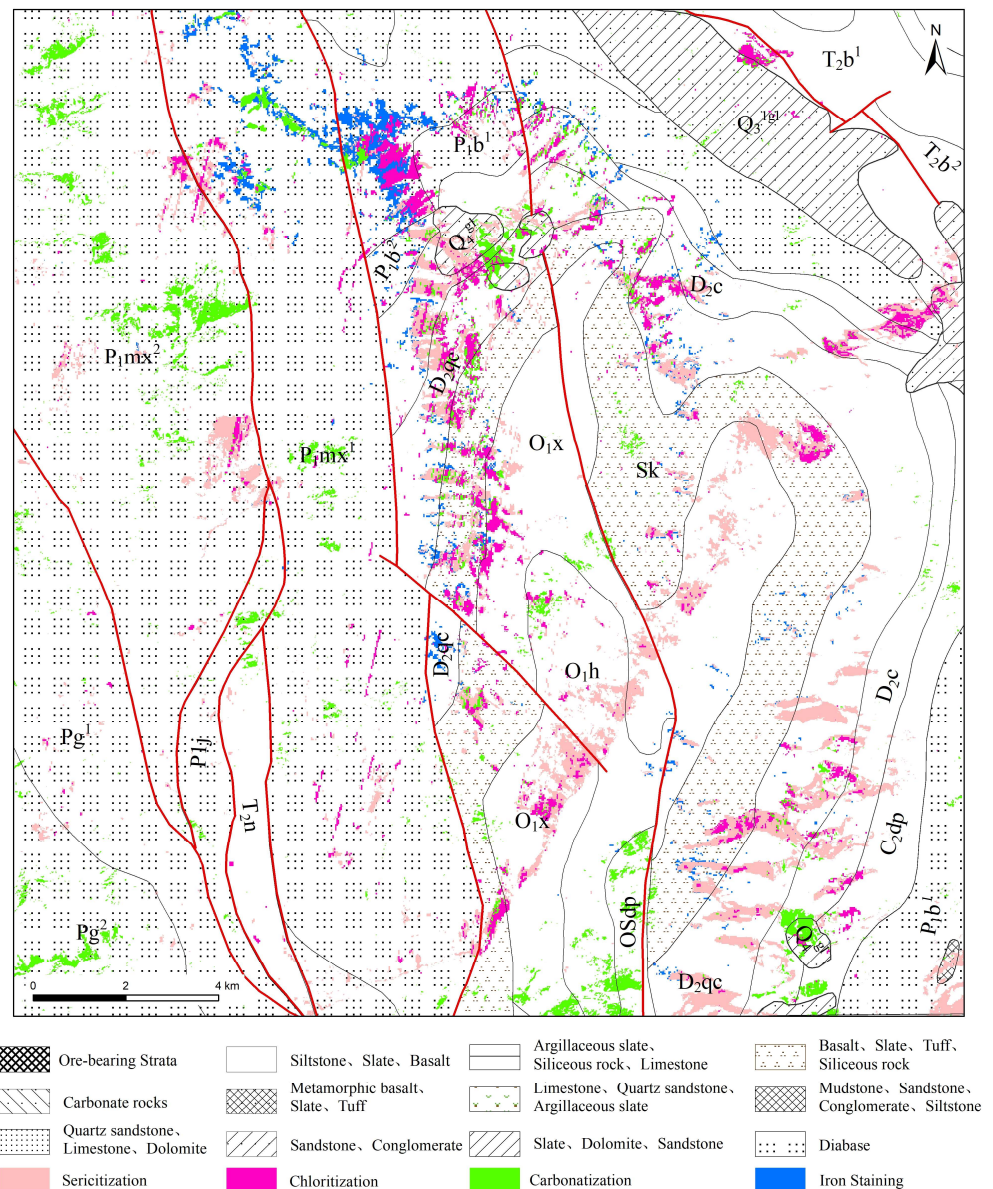
Figure 14. Comparison of alteration results and stratigraphy.

Comparing the geological map with remote sensing mapping highlights significant and minor differences, which supplements traditional fieldwork by revealing detailed information that may be challenging to detect otherwise. The extraction results in areas with sparse vegetation, no snow cover, and minimal shadow provide supplementary insights to existing geological maps.

5.4. Comparison of Alteration Extraction Results from ASTER and ZY1-02D

The ASTER data, acquired in October 2005, and ZY1-02D data, acquired in October 2021, span a significant 16-year period. Despite both images being captured in October, there is a stark contrast in snow coverage in high-altitude areas. The ASTER image shows extensive snow cover, whereas in the ZY1-02D image, snow covers only parts of the mountaintops, with many areas remaining bare. This disparity explains the considerable differences in results obtained from the two datasets.

This study utilized ASTER and ZY1-02D data to extract alteration information, including iron staining (limonite), chloritization (chlorite), sericitization (sericite), and carbonate alteration (calcite). By summarizing the distinct characteristics of these alteration types

extracted using the two datasets and methods, we can roughly compare the advantages and disadvantages of both results in the local area. ASTER's alteration information covers a larger and broader distribution area, often occurring in large patches (Figure 7), while ZY1-02D provides more refined information with smaller areas (Figure 8), often in blocky distributions. In areas of relatively concentrated distribution, there are sometimes blank areas within ZY1-02D's data, whereas ASTER tends to classify entire concentrated regions uniformly as one type of alteration. Fieldwork confirms that ZY1-02D's alteration information aligns more closely with the validation results on the ground, thus demonstrating its finer accuracy.

The wavelength ranges of ASTER (0.52–11.65 µm) and ZY1-02D (0.396–2.501 µm) also contribute to the differences in their mineral detection capabilities. Minerals with spectral features beyond 2.501 µm cannot be effectively identified using ZY1-02D data, while ASTER can cover these minerals well, including quartz, which falls within ASTER's thermal infrared band. However, due to ASTER's lower spatial resolution (90 m), quartz alteration appears coarse and may exhibit noticeable striping. ZY1-02D excels in spectral resolution, with a 10 nm resolution in the VNIR range and 20 nm in the SWIR range, enabling more precise selection of characteristic spectral bands. Additionally, its continuous wavelength coverage (0.396–2.501 µm) ensures no spectral gaps, enhancing its utility for detailed mineralogical studies.

6. Conclusions

This article employed multispectral and hyperspectral remote sensing imagery, specifically utilizing ASTER and ZY1-02D data, to interpret geological structures and identify prospective target areas in the Mahuaping Mine area of Shangri-La. Our methods included visual interpretation, principal component analysis (PCA), and spectral angle mapping (SAM). These techniques successfully identified linear and circular geological structures as well as minerals with distinctive spectral signatures. The structural interpretation in this project identified a total of 34 faults trending in the NE direction, 7 faults trending approximately N-S, and 14 faults trending in the NW direction. There are three volcanic rings, three tectonic rings, and one concealed rock mass ring.

The interpretation of linear and circular structures was refined using ASTER false-color imagery, while both ASTER and ZY1-02D data aided in identifying surface lithology features such as iron staining, chloritization, sericitization, and carbonatization. Anomalies in alteration patterns were mapped, pinpointing five potential target areas characterized by pronounced alteration signals indicative of significant mineralization potential. Each target area contains multiple sets of diverse alteration information, with faults intersecting or surrounding the area. These faults play a crucial role in ore hosting and mineralization. These favorable mineralization conditions indicate high potential for exploration in these regions. These target areas will be the primary focus of subsequent field exploration efforts.

To validate these findings, our fieldwork encompassed 25 sampling points, involving spectral scans and microscopic analysis. The spectral curves for minerals like chlorite, sericite, calcite, and pyrite closely matched those in the USGS spectral library. Polarized microscopy confirmed the presence of minerals such as quartz, tourmaline, sericite, and pyrite, with the direct discovery of scheelite, affirming the accuracy of the identified target areas. Furthermore, we compared the results with known lithological units, and corresponding altered minerals can be well matched with respective rock types in the strata, showing good agreement. The comparison of the results from the two datasets considered factors such as the temporal consistency, quality, and resolution of the imagery results. Based on field validation, the results obtained from ZY1-02D are deemed more reliable in this region.

The results indicate that preliminary remote sensing surveys are of significant importance. When used appropriately, they can reduce the required manpower and resources, and enhance the efficiency of mineral exploration operations. However, some igneous minerals with similar spectral features are difficult to distinguish and identify. Additionally, minor minerals with low concentrations exhibit weak alteration anomaly signals. Com-

bined with issues such as image noise and dense surface vegetation cover that make the penetration of electromagnetic waves challenging, as well as persistent snow cover in some areas, fieldwork becomes particularly important under these circumstances.

References

1. Ye, T.Z. Theoretical Framework of Methodology of Deposit Modeling and Integrated Geological Information for Mineral Resource Potential Assessment. *J. Jilin Univ.* **2013**, *43*, 1053–1072, (In Chinese with English abstract).
2. Adams, J.B. Visible and near-infrared diffuse reflectance spectra of pyroxenes as applied to remote sensing of solid objects in the solar system. *J. Geophys. Res.* **1974**, *79*, 4829–4836. [CrossRef]
3. Adams, J.B.; Filice, A.L. Spectral reflectance 0.4 to 2.0 microns of silicate rock powders. *J. Geophys. Res.* **1967**, *72*, 5705–5715. [CrossRef]
4. Rowan, L.C.; Mars, J.C.; Simpson, C.J. Lithologic Mapping of the Mordor, NT, Australia Ultramafic Complex by Using the Advanced Spaceborne Thermal Emission and Reflection Radiometer (ASTER). *Remote Sens. Environ.* **2005**, *99*, 105–126. [CrossRef]
5. Fraser, S.J.; Green, A.A. A Software Defoliant for Geological Analysis of Band Ratios. *Int. J. Remote Sens.* **1987**, *8*, 525–532. [CrossRef]
6. Loughlin, W.P. Principal Component Analysis for Alteration Mapping. *Photogramm. Eng. Remote Sens.* **1991**, *57*, 1163–1169.
7. Johnson, P.E.; Smith, M.O.; Adams, J.B. Simple Algorithms for Remote Determination of Mineral Abundances and Particle Sizes from Reflectance Spectra. *J. Geophys. Res. Planets* **1992**, *97*, 2649–2657. [CrossRef]
8. Kumar, C.; Chatterjee, S.; Oommen, T.; Guha, A. Automated lithological mapping by integrating spectral enhancement techniques and machine learning algorithms using AVIRIS-NG hyperspectral data in Gold-bearing granite-greenstone rocks in Hutti, India. *Int. J. Appl. Earth Obs. Geoinf.* **2020**, *86*, 102006. [CrossRef]
9. Van Der Meer, F.D.; Van Der Werff, H.M.A.; Van Ruitenbeek, F.J.A.; Hecker, C.A.; Bakker, W.H.; Noomen, M.F.; Van Der Meijde, M.; Carranza, E.J.M.; De Smeth, J.B.; Woldai, T. Multi-and hyperspectral geologic remote sensing: A review. *Int. J. Appl. Earth Obs. Geoinf.* **2021**, *14*, 112–128. [CrossRef]
10. Sun, Y.; Liu, J.J.; Zhai, D.G.; Liu, Z.J.; Zhang, F.F.; Zhao, Y.J.; Liu, P.F.; Wang, Z.T. Alteration minerals mapping and identification of gold mineralization belt based on ZY1-02D hyperspectral data in the Toudiaoquan-Nandatan area, Ganse Province. *Geol. Prospect.* **2022**, *58*, 399–409. (In Chinese)
11. Amer, R.; Kusky, T.; Ghulam, A. Lithological Mapping in the Central Eastern Desert of Egypt Using ASTER Data. *J. Afr. Earth Sci.* **2010**, *56*, 75–82. [CrossRef]
12. Xiong, Y.; Khan, S.D.; Mahmood, K.; Sisson, V.B. Lithological Mapping of Bela Ophiolite with Remote-Sensing Data. *Int. J. Remote Sens.* **2011**, *32*, 4641–4658. [CrossRef]
13. Lobo, A.; Garcia, E.; Barroso, G.; Martí, D.; Fernandez-Turiel, J.L.; Ibáñez-Insa, J. Machine Learning for Mineral Identification and Ore Estimation from Hyperspectral Imagery in Tin–Tungsten Deposits: Simulation under Indoor Conditions. *Remote Sens.* **2021**, *13*, 3258. [CrossRef]
14. Pei, C.-K.; Fu, J. Status and prospect of hyperspectral remote sensing technique in rock and mineral identification. *World Nuclear Geosci.* **2007**, *24*, 32–38, (In Chinese with English abstract).
15. Wei, J.; Ming, Y.-F.; Han, L.-S.; Ren, Z.-L.; Guo, Y.-M. Remote sensing identification method of mineral information based on matching of multispectral characteristic parameters. *Spectrosc. Spectr. Anal.* **2015**, *35*, 2862–2866. (In Chinese)
16. Mohammadi, N.M.; Hezarkhani, A. Application of Support Vector Machine for the Separation of Mineralised Zones in the Takht-e-Gonbad Porphyry Deposit, SE Iran. *J. Afr. Earth Sci.* **2018**, *143*, 301–308. [CrossRef]
17. Ordóñez-Calderón, J.C.; Gelcich, S. Machine Learning Strategies for Classification and Prediction of Alteration Facies: Examples from the Rosemont Cu-Mo-Ag Skarn Deposit, SE Tucson Arizona. *J. Geochem. Explor.* **2018**, *194*, 167–188. [CrossRef]
18. Carrino, T.A.; Crósta, A.P.; Toledo, C.L.B.; Silva, A.M. Hyperspectral Remote Sensing Applied to Mineral Exploration in Southern Peru: A Multiple Data Integration Approach in the Chapi Chiara Gold Prospect. *Int. J. Appl. Earth Obs. Geoinf.* **2018**, *64*, 287–300. [CrossRef]

19. Cheng, J.L.; Yang, L.Y.; Cui, Z.L.; Zhang, X.H. *Mineral Geology of China · Yunnan Volume · Tin and Tungsten Minerals*; Yunnan Institute of Geology and Mineral Exploration: Kunming, China, 2019; pp. 245–257. (In Chinese)

20. Ran, M.J.; Zhong, K.H.; Yang, J.G.; Luo, M.F. *Geochemistry and Its Genesis Implications of Beryllium and Tungsten Deposit in Mahuaping of Shangri-La, Yunnan*; Sichuan Nonferrous Metals: Chengdu, China, 2015; pp. 42–45, (In Chinese with English abstract).

21. Zhou, Z.; Wen, H.; Qin, C.; Liu, L. Geochemical and isotopic evidence for a magmatic-hydrothermal origin of the polymetallic vein-type Zn-Pb deposits in the northwest margin of Jiangnan Orogen, South China. *Ore Geol. Rev.* **2017**, *86*, 673–691. [CrossRef]

22. Jiang, S.; Woodhead, J.; Yu, J.; Pan, J.; Liao, Q.; Wu, N. A reconnaissance of Cu isotopic compositions of hydrothermal vein-type copper deposit Jinman, Yunnan, China. *Chin. Sci. Bull.* **2002**, *47*, 249–251. [CrossRef]

23. Han, C.C.; Zhang, X.B.; Wu, S.S.; Liu, Y.T. The Magmatic-Hydrothermal Ore-Forming Processes of the Tonggou Cu-Zn Deposit, NW China: Constraints from Magnetite Chemistry and Fluid Inclusions. *Minerals* **2022**, *12*, 485. [CrossRef]

24. Ma, J.; Tao, Y.; He, D.F.; Xiong, F. The Ore-Forming Age and Fluid Inclusion Characteristics of the Mahuaping Tungsten-Beryllium Deposit in Yunnan Province. *Bull. Mineral. Geochem.* **2020**, *39*, 223–232. [CrossRef]

25. Xiong, F.; Tao, Y.; Deng, X.Z. Characteristics of fluid inclusions and genetic analysis of the Mahuaping tungsten-beryllium deposit in Yunnan. *Acta Mineral. Sin.* **2015**, *35*, 353–354. [CrossRef]

26. Elaaraj, A.; Lhachmi, A.; Tabyaoui, H.; Alitane, A.; Varasano, A.; Hitouri, S.; El Yousfi, Y.; Mohajane, M.; Essahlaoui, N.; Gueddari, H.; et al. Remote Sensing Data for Geological Mapping in the Saka Region in Northeast Morocco: An Integrated Approach. *Sustainability* **2022**, *14*, 15349. [CrossRef]

27. Pan, Z.; Liu, J.; Ma, L.; Chen, F.; Zhu, G.; Qin, F.; Zhang, H.; Huang, J.; Li, Y.; Wang, J. Research on Hyperspectral Identification of Altered Minerals in Yemaquan West Gold Field, Xinjiang. *Sustainability* **2019**, *11*, 428. [CrossRef]

28. Nafigin, I.O.; Ishmukhametova, V.T.; Ustinov, S.A.; Minaev, V.A.; Petrov, V.A. Geological and Mineralogical Mapping Based on Statistical Methods of Remote Sensing Data Processing of Landsat-8: A Case Study in the Southeastern Transbaikalia, Russia. *Sustainability* **2022**, *14*, 9242. [CrossRef]

29. Dong, T.; Du, B.; Duan, Z.Y.; Cao, X.M.; Song, X.F.; Dong, H.G.; Zhang, Y.M.; Li, B. Metallogenic regularity and prospecting direction of tungsten deposits in Shangri-La area, NW Yunnan Province, China. *Sediment. Geol. Tethyan Geol.* **2022**, *42*, 62–74, (In Chinese with English abstract).

30. Ran, M.J.; Zhong, K.H.; Li, F.Y.; Luo, M.F.; Liu, Z.C.; Tang, J.X. *Analysis of the Tectonic of Deposit and the Age of Mineralization in Mahuaping of Shangri-La in Yunnan*; Sichuan Nonferrous Metals: Chengdu China, 2011; pp. 21–27, (In Chinese with English abstract).

31. Rowan, L.C.; Mars, J.C. Lithologic mapping in the Mountain Pass, California area using Advanced Spaceborne Thermal Emission and Reflection Radiometer (ASTER) data. *Remote Sens. Environ.* **2003**, *84*, 350–366. [CrossRef]

32. Mahdi, A.M.; Eldosouky, A.M.; Elkhateeb, S.O.; Youssef, A.M.; Saad, A.A. Integration of remote sensing and geophysical data for the extraction of hydrothermal alteration zones and lineaments; Gabal Shilman basement area, Southeastern Desert, Egypt. *J. Afr. Earth Sci.* **2022**, *194*, 104640. [CrossRef]

33. Abubakar, A.J.; Hashim, M.; Pour, A.B. Identification of hydrothermal alteration minerals associated with geothermal system using ASTER and Hyperion satellite data: A case study from Yankari Park, NE Nigeria. *Geocarto Int.* **2019**, *34*, 597–625. [CrossRef]

34. Ghosh, U.K.; Naik, K.K.; Kesari, M.P. Digital image processing of multispectral ASTER imagery for delineation of alteration and related clay minerals in Sakoli belt: Maharashtra—A case study. *J. Geol. Soc. India* **2016**, *88*, 464–470. [CrossRef]

35. Zhao, Z.F. *Study on Remote Sensing Anomaly Information of Mineralization*; China University of Geosciences: Beijing, China, 2008; (In Chinese with English abstract).

36. Xu, T.; Liu, X.F.; Zhang, J.F.; Yang, F.F. Research progress of quartz vein type tungsten ore mineralization. *Contrib. Geol. Miner. Resour. Res. Contr. Geol Min. Resour. Res.* **2019**, *34*, 196–200. (In Chinese)

37. Pour, A.B.; Hashim, M. Identifying areas of high economic-potential copper mineralization using ASTER data in the Urumieh–Dokhtar Volcanic Belt, Iran. *Adv. Space Res.* **2012**, *49*, 753–769. [CrossRef]

38. Hegab, M.A.E.R.; Mousa, S.E.; Salem, S.M.; Farag, K.; GabAllah, H. Gold-related Alteration Zones Detection at the Um Balad Area, Egyptian Eastern Desert, using Remote Sensing, Geophysical, and GIS Data Analysis. *J. Afr. Earth Sci.* **2022**, *196*, 104715. [CrossRef]

39. Zhang, M.L. Principal component analysis in gold mine alteration information extraction. *Remote Sens. Technol. Appl.* **1996**, *11*, 2–7. (In Chinese) [CrossRef]

40. Li, C.G.; Zhang, Y.J. *The Principal Component Analysis Method was Used to Extract Remote Sensing Information of Copper Mineralization Alteration in Lanping Area of Lancang River*; Remote Sensing for Land & Resources: Beijing, China, 1997; pp. 22–32. (In Chinese)

41. Wang, R.D.; Xing, L.X. Remote sensing extraction method of alteration information of ore deposit. *World Geol.* **2000**, *19*, 397–401. (In Chinese)

42. Abdelkareem, M.; El-Baz, F. Characterizing hydrothermal alteration zones in Hamama area in the central Eastern Desert of Egypt by remotely sensed data. *Geocarto Int.* **2018**, *33*, 1307–1325. [CrossRef]

43. Gabr, S.S.; Hassan, S.M.; Sadek, M.F. Prospecting for new gold-bearing alteration zones at El-Hoteib area, South Eastern Desert, Egypt, using remote sensing data analysis. *Ore Geol. Rev.* **2015**, *71*, 1–13. [CrossRef]

44. Honarpazhouh, J.; Hassanipak, A.A.; Seifpanahi, S.K. Integration of Stream Sediment Geochemical and Aster Data for Porphyry Copper Deposit Exploration in Khatun Abad, North West of Iran/Integracja geochemicznych danych o osadach dennych oraz danych pozyskanych z systemu aster do poszukiwań geologicznych w rejonie złóż miedzi porfirytowej w khatun abad, w północno-zachodniej części iranu. *Arch. Min. Sci.* **2013**, *58*, 37–54.

45. Kruse, F.A.; Lefkoff, A.B.; Boardman, Y.J.; Heidebrecht, K.B.; Shapiro, A.T.; Barloon, P.J.; Goetz, A.F.H. The Spectral Image Processing System (SIPS) Interactive Visualization and Analysis of Imaging Spectrometer Data. *Remote Sens. Environ.* **1993**, *44*, 145–165. [CrossRef]

46. Zhang, Y.J.; Zeng, C.M.; Chen, W. Research and application of remote sensing anomaly extraction method for ETM~+(TM) alteration: Method selection and technical process. *Remote Sens. Land Resour.* **2003**, *2*, 44–49, (In Chinese with English abstract).

47. Yonezawa, C. Maximum likelihood classification combined with spectral angle mapper algorithm for high resolution satellite imagery. *Int. J. Remote Sens.* **2007**, *28*, 3729–3737. [CrossRef]

48. Qiu, F.; Abdelsalam, M.; Thakkar, P. Spectral analysis of ASTER data covering part of the Neoproterozoic Allaqi-Heiani suture, Southern Egypt. *J. Afr. Earth Sci.* **2006**, *44*, 169–180. [CrossRef]

49. Honarmand, M.; Ranjbar, H.; Shahabpour, J. Application of Principal Component Analysis and Spectral Angle Mapper in the Mapping of Hydrothermal Alteration in the Jebal-Barez Area, Southeastern Iran: Hydrothermal alteration mapping. *Resour. Geol.* **2012**, *62*, 119–139. [CrossRef]

50. Shahriari, H.; Ranjbar, H.; Honarmand, M.; Carranza, E.J.M. Selection of Less Biased Threshold Angles for SAM Classification Using the Real Value–Area Fractal Technique. *Resour. Geol.* **2014**, *64*, 301–315. [CrossRef]

51. Krupnik, D.; Khan, S.D. High-Resolution Hyperspectral Mineral Mapping: Case Studies in the Edwards Limestone, Texas, USA and Sulfide-Rich Quartz Veins from the Ladakh Batholith, Northern Pakistan. *Minerals* **2020**, *10*, 967. [CrossRef]

52. Hubbard, B.E.; Gallegos, T.J.; Stengel, V. Mapping Abandoned Uranium Mine Features Using Worldview-3 Imagery in Portions of Karnes, Atascosa and Live Oak Counties, Texas. *Minerals* **2023**, *13*, 839. [CrossRef]

53. Kayet, N.; Pathak, K.; Singh, C.P.; Chowdary, V.M.; Bhattacharya, B.K.; Kumar, D.; Kumar, S.; Shaik, I. Vegetation health conditions assessment and mapping using AVIRIS-NG hyperspectral and field spectroscopy data for-environmental impact assessment in coal mining sites. *Ecotoxicol. Environ. Saf.* **2022**, *239*, 113650. [CrossRef]

54. Lotfi, M.; Arefi, H.; Bahroudi, A. Investigating alteration zone mapping using EO-1 Hyperion imagery and airborne geophysics data. *J. Min. Environ.* **2020**, *11*, 405–417. [CrossRef]

55. Mehdikhani, B.; Imamalipour, A. ASTER-Based Remote Sensing Image Analysis for Prospection Criteria of Podiform Chromite at the Khoy Ophiolite (NW Iran). *Minerals* **2021**, *11*, 960. [CrossRef]

56. Pournamdari, M.; Hashim, M.; Pour, A.B. Application of ASTER and Landsat TM Data for Geological Mapping of Esfandagheh Ophiolite Complex, Southern I ran. *Resour. Geol.* **2014**, *64*, 233–246. [CrossRef]

57. Wang, Y.L.; Wang, R.; Yan, Z.Q.; Zhang, X.M.; Li, X.L.; Xu, C.L. Extraction of structural alteration information and prospecting prediction in Delong area of Qinghai Province using GF-2 and ASTER data. *Remote Sens. Nat. Resour.* **2023**, *36*, 1–10. (In Chinese)

58. Wu, Z.C.; Guo, F.S.; Liu, L.Q.; Xie, C.F.; Jiang, Y.B. Application of remote sensing alteration anomaly extraction with the method of composite algorithm based on TM/ETM images. *Geol. Explor.* **2013**, *49*, 511–522. (In Chinese)

59. Zhang, C.; Ye, F.W.; Xu, Q.J.; Liu, H.C.; Meng, S. Mineral mapping and analysis of alteration characteristics using airborne hyperspectral remote sensing data in the Baiyanghe uranium and beryllium ore district, Xinjiang. *Remote Sens. Land Resour.* **2017**, *29*, 161–166. (In Chinese)

60. Liang, S.N.; Gan, P.P.; Yan, B.K.; Wei, H.Y.; Xiao, C.C. Study on the relationship between mineral composition and spectral characteristics of chlorite. *Spectrosc. Spectr. Anal.* **2014**, *34*, 1764–1768. (In Chinese)

61. Zhai, W.Y.; Chen, L.; Xu, Y.X.; Kong, X.Y. Quantitative inversion of influencing factors of carbonate minerals by spectral absorption depth and application analysis. *Spectr. Spectr. Anal.* **2021**, *41*, 2227–2232. (In Chinese)